STATISTICS, OPTIMIZATION AND INFORMATION COMPUTING
Stat., Optim. Inf. Comput., Vol. **x**, Month 202x, pp 1–26.
Published online in International Academic Press (www.IAPress.org)

A Wavelet-Based Architecture for Efficient ECG Signal Denoising

Shelan Kamal Ahmed[1,2*], Serwan Ali Mohammed[2], Ahmed Khorsheed Mohammed[2]

[1] *Department of Energy Engineering, Duhok Polytechnic University, Iraq*
[2] *Department of Electrical and Computer Engineering, University of Duhok, Iraq*

Abstract An electrocardiogram (ECG) is one of the most important biomedical signals for the detection and diagnosis of heart arrhythmias. As an interpretable biomedical signal, the ECG is subject to various interferences and noise sources, such as baseline wander, 50 Hz power-line interference, and additive white Gaussian noise, all of which may obscure vital diagnostic information and distort clinically relevant features. This study aims to develop an efficient, lightweight, and morphology-preserving denoising method for ECG signals that can suppress multiple noise sources simultaneously.
This paper proposes a unified Discrete Wavelet Transform (DWT)-based architecture that combines frequency-selective subband filtering with adaptive soft thresholding and multilevel baseline wander removal. The method was evaluated using both synthetic ECG signals and real recordings from the MIT-BIH Arrhythmia Database. Performance was assessed using SNR improvement (SNRimp), correlation coefficient (CC), mean square error (MSE), and percentage root mean square difference (PRD). Using the bior6.8 wavelet with soft thresholding, the proposed method achieved SNR improvement up to 19.67 ± 0.37 dB at SNRi = -5 dB and 15.29 ± 0.33 dB at SNRi = 0 dB, with corresponding CC values of 0.9828 ± 0.0019 and 0.9851 ± 0.0017, respectively, demonstrating strong noise suppression while preserving ECG morphology. Across all tested SNR levels (-5 to 10 dB), the method consistently maintained CC ≥ 0.98 and PRD below 18% for synthetic data. On challenging real MIT-BIH arrhythmia records (104, 105, 108, 114, 208, 228), the method achieved output SNR up to 20.16 ± 0.58 dB and CC in the range 0.98–0.995, while preserving key diagnostic features such as the QRS complex and ST-segment. Performance degraded only in record 114 due to severe motion artifacts, which is consistent with prior studies. Compared with representative traditional and recent deep-learning denoising approaches, the proposed DWT-based architecture achieved superior or competitive performance while remaining computationally efficient and training-free, making it suitable for real-time and wearable ECG applications. Overall, the results confirm that the proposed method provides a robust, unified, and clinically reliable solution for multi-noise ECG denoising.

Keywords Clean Synthetic ECG Signal, Denoising ECG Signals, Power-Line Interference, Baseline Wander, Wavelet Transform

DOI: 10.19139/soic-2310-5070-3155

1. Introduction

Electrocardiogram (ECG) signals represent the electrical activity of the heart and are essential for diagnosing cardiovascular disorders. However, ECG recordings are commonly corrupted by multiple noise sources such as baseline wander, power-line interference, and additive white Gaussian noise (AWGN), which can degrade QRS morphology, distort ST-segment deviation, and result in diagnostic errors [1, 2]. Therefore, efficient ECG denoising is critical for preserving high-quality diagnostic information.

1.1. Motivation and Background

The Discrete Wavelet Transform (DWT) is one of the most effective techniques for ECG denoising due to its strong time–frequency localization capability[3, 4]. By decomposing ECG signals into multi-resolution subbands,

*Correspondence to: Shelan Kamal Ahmed (Email: shelan.kamal@dpu.edu.krd).
Duhok Polytechnic University, Duhok, Iraq.

ISSN 2310-5070 (online) ISSN 2311-004X (print)

DWT enables noise suppression precisely where different noise sources dominate. Unlike the Short-Time Fourier Transform (STFT), which applies a fixed window across frequencies, DWT adapts to abrupt cardiac activities such as QRS complexes while preserving slow waveform components like the ST-segment. Furthermore, compared to empirical mode decomposition (EMD) and nonlinear adaptive filtering methods, DWT avoids mode-mixing problems and offers significantly lower computational complexity, making it highly suitable for real-time and wearable ECG monitoring applications[5]. Recently, deep-learning approaches such as recurrent neural networks and convolutional autoencoders have also been explored for ECG denoising, demonstrating promising performance in noise reduction tasks[6], [7].

1.2. Related Work and Challenges

A wide range of ECG denoising methods have been proposed in the literature. Wavelet-based techniques and adaptive filtering remain among the most commonly adopted approaches due to their efficiency in noise suppression. Filter bank techniques [8, 9] have shown potential in enhancing P and R wave representation. However, empirical mode decomposition (EMD)-based approaches [10, 11, 12] may suffer from mode-mixing effects, sensitivity to noise, and high computational complexity, making them less suitable for real-time scenarios. DWT-based methods continue to be widely used because they achieve effective noise reduction while maintaining ECG waveform morphology. Numerous studies have investigated different wavelet families, decomposition levels, and thresholding techniques [13, 14, 15]. The performance of DWT depends strongly on these parameter selections. Nevertheless, most existing solutions are designed to remove only a single type of noise (e.g., baseline wander or power-line interference), and only a few works have aimed to jointly eliminate multiple noise sources simultaneously. Moreover, the majority of previous studies do not provide sufficient justification for selecting optimal wavelet parameters or considering computational efficiency for real-time ECG monitoring. Therefore, a unified, morphology-preserving, and computationally efficient approach remains highly important for practical biomedical applications. For example, [16]proposed a hybrid framework combining wavelets, variational mode decomposition, and nonlocal means filtering to suppress multiple noise sources, while [17] developed a Fourier-series model for generating realistic synthetic ECG signals widely used in denoising studies. More recently, [18] provided a comparative evaluation of filtration techniques with emphasis on stationary wavelet transform, whereas [19] introduced an adaptive layer-dependent wavelet thresholding scheme for ECG and cardiorespiratory signals. Similarly, [20] integrated particle swarm optimization with wavelet thresholding to enhance denoising performance. These studies collectively highlight the continued relevance of wavelet-domain techniques for reliable ECG preprocessing. Moreover, stationary and enhanced DWT-based frameworks have demonstrated robustness against EMG interference and non-invasive measurement noise [21, 22]. These findings highlight the continued relevance of wavelet-domain techniques as a foundation for reliable ECG preprocessing. However, existing denoising approaches still suffer from several limitations: (i) they typically target only one noise source at a time, which is not suitable for real-world ECG recordings; (ii) morphology distortion can occur using standard wavelet thresholding; and (iii) computational complexity and real-time deployment thresholding are investigated. Therefore, a unified, morphology-preserving, and computationally efficient denoising architecture remains an open research need, particularly in wearable and bedside cardiac monitoring systems.

1.3. Research Objectives

The primary objective of this research is to develop a unified DWT-based denoising architecture capable of simultaneously suppressing baseline wander, 50 Hz power-line interference, and additive white Gaussian noise (AWGN) while preserving clinically important ECG morphology. A secondary objective is to evaluate the computational efficiency of the proposed approach to determine its suitability for near real-time wearable ECG monitoring. To clearly define the performance expectations, the following quantitative success criteria are established:

- Correlation coefficient (CC) ≥ 0.98
- Percent Root-mean-square Difference (PRD) $\leq 20\%$
- Signal-to-Noise Ratio (SNR) improvement ≥ 10 dB

- Processing time ≤ 3 seconds per 4096-sample segment

1.4. Research Questions

To support the formulation and evaluation of the proposed denoising architecture, the following research questions are investigated:

- **RQ1:** Which wavelet family provides the best balance between noise reduction and preservation of ECG morphology?
- **RQ2:** What decomposition level is theoretically and experimentally optimal for isolating each type of noise?
- **RQ3:** Does the proposed unified architecture outperform sequential application of noise-specific filtering approaches?
- **RQ4:** Is the denoising performance consistent across different ECG morphologies and noise conditions?

1.5. Contributions

The main contributions of this paper are summarized as follows:

- A unified DWT-based architecture is proposed to jointly suppress multiple ECG noise sources including baseline wander, power-line interference, muscle artifacts, and white Gaussian noise.
- The method effectively preserves important ECG morphological features such as QRS complexes and ST-segment behavior.
- A comprehensive evaluation is performed on both synthetic and real ECG signals from the MIT-BIH database, demonstrating superior denoising performance over existing techniques.
- The proposed approach exhibits low computational complexity, making it suitable for real-time and wearable ECG monitoring systems.

1.6. Organization

The remainder of this paper is organized as follows. Section 2 describes the fundamentals of ECG denoising, the characteristics of noise sources, and essential preprocessing techniques. Section 3 presents the theoretical background and wavelet-based methodology. Section 4 details the proposed denoising architecture and experimental setup. Section 5 reports the results and provides detailed performance analysis. Finally, Section 6 concludes the paper and outlines future research directions.

2. ECG denoising prerequisite

2.1. Generating Clean Synthetic ECG Signal

To evaluate ECG denoising performance, comparisons between the denoised signal and a clean reference signal are necessary. Therefore, a clean synthetic ECG signal is generated first, and different noise types are later added to it to create controlled noisy signals. Several approaches have been proposed for generating realistic ECG models [23, 24, 25, 26, 27]. One widely used technique is Fourier series modeling because the ECG waveform is quasi-periodic and can be represented mathematically as a periodic function.

In this study, a clean synthetic ECG signal is generated at a sampling frequency of $f_s = 360$ Hz, matching the MIT-BIH database. The waveform consists of repeating P-wave, QRS complex, and T-wave components that mimic normal sinus rhythm. Fig. 3 shows the clean synthetic ECG and its frequency spectrum.

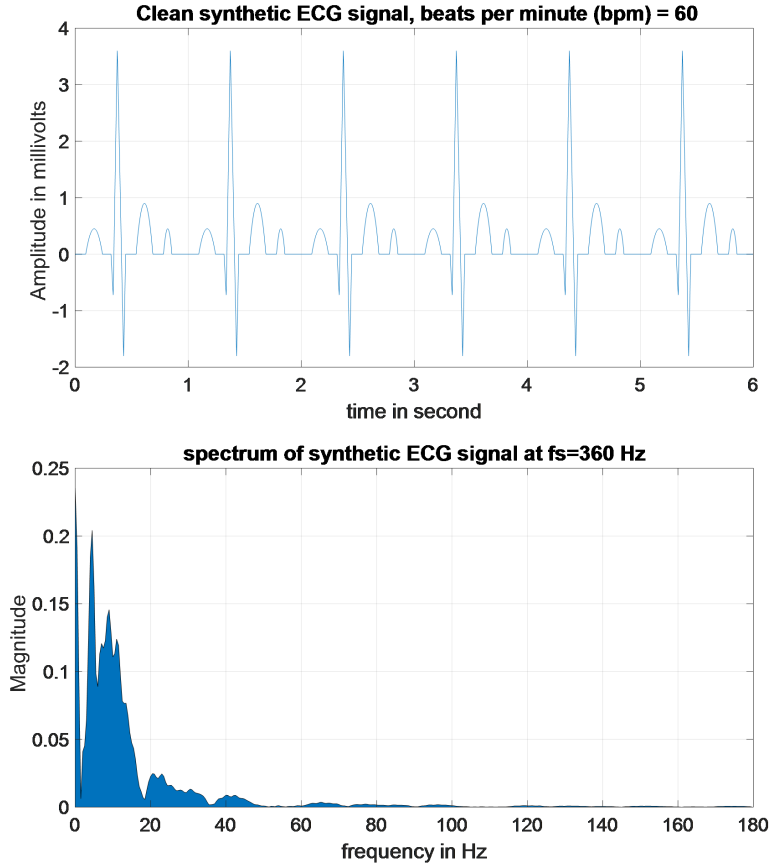

Figure 1. Clean synthetic ECG signal in the time domain and its corresponding frequency spectrum at $f_s = 360\,\text{Hz}$.

To provide a clear and reproducible synthesis framework, Fig. 2 summarizes the major steps involved in generating the clean synthetic ECG signal based on Fourier series modeling. Each part of the ECG waveform P-wave, QRS complex and T-wave are mathematically represented and repeated according to the heart rate to produce a periodic simulated beat.

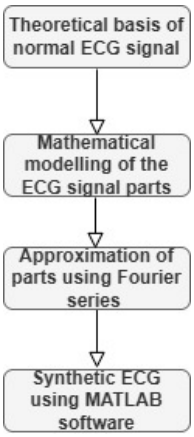

Figure 2. Flowchart of the synthetic ECG generation procedure based on Fourier series modeling.

The synthetic ECG was generated as a periodic waveform representing normal sinus rhythm at 72 bpm, sampled at 360 Hz to match the MIT-BIH database. The durations and amplitudes of P-QRS-T components were selected within standard physiological ranges to ensure realistic morphology, as shown in Table 1.

Table 1. Physiological and signal parameters of the synthetic ECG used in this study.

Parameter	**Description**	**Value used in this study**
Sampling frequency (f_s)	ECG sampling rate	360 Hz
Heart rate (HR)	Beats per minute of modeled signal	72 bpm
RR interval	Duration between successive R-peaks	833 ms
P-wave amplitude	Height of P wave	≈ 0.2 mV
P-wave duration	Length of P wave	$\approx$ 80–120 ms
QRS amplitude	Peak-to-peak height	$\approx$ 0.5–1.0 mV
QRS duration	Width of the complex	$\approx$ 80–120 ms
T-wave amplitude	Height of T wave	$\approx$ 0.1–0.3 mV
T-wave duration	Length of T wave	$\approx$ 150–250 ms

2.2. Types of noise contaminating ECG signals

Electrocardiogram readings often have noise from internal and external sources, which can change how look and make diagnosis harder. Common interference types include baseline wander, power line noise, electromyographic (EMG) noise and motion artifacts. Baseline wander, a low-frequency issue, usually comes from breathing, body movement, or slow changes in electrode potential. Power-line interference, a medium-frequency issue, comes from the power grid. EMG noise has high-frequency changes due to muscle activity while motion artifacts happen when electrodes move on the skin. Each noise type has its own spectral qualities that we can use to create good filtering and denoising techniques. Also, additive white Gaussian noise (AWGN) is a basic noise model in signal processing that mimics the random disturbances common in biomedical setups.

2.3. Performance metrics

To compare various denoising approaches, five standard metrics are employed.

(a) The input mean-square-error (mse_i) is calculated as the average of the squared differences between the original clean ECG signal $x(k)$ and the corrupted ECG signal $y(k)$ with N size. The mse_i is given by:

$$mse_i = \frac{1}{N}\sum_{k=0}^{N-1}(x(k) - y(k))^2 \tag{1}$$

(b) The output mean-square-error (mse_o) is calculated as the average of the squared differences between the original clean ECG signal $x(k)$ and the denoised ECG signal $x_r(k)$ with size N. This mse_o is given by:

$$mse_o = \frac{1}{N}\sum_{k=0}^{N-1}(x(k) - x_r(k))^2 \tag{2}$$

The mean-square error evaluates the variance between the real ECG signal and the denoised ECG signal. A lower mean-square error means a smaller difference.

(c) Improved signal-to-noise ratio ($impdB$SNR) measures the amount of improvement in signal quality when denoising processes are employed[28, 29]. The $impdB$ is defined as:

$$impdB = SNR_o - SNR_i \tag{3}$$

Where

$$SNR_i = 10\log_{10}\left(\frac{\sum_{k=0}^{N-1}(x(k))^2}{\sum_{k=0}^{N-1}(x(k)-y(k))^2}\right) \tag{4}$$

$$SNR_o = 10\log_{10}\left(\frac{\sum_{k=0}^{N-1}(x(k))^2}{\sum_{k=0}^{N-1}(x(k)-x_r(k))^2}\right) \tag{5}$$

It should be mentioned that SNR measures the quality of denoised ECG signal. The higher output SNR, the better the denoising performance.

(d) The correlation coefficient (r) of $x(k)$ and $y_r(k)$ is a measure of their linear dependence and is defined as

$$CC = \frac{1}{N}\sum_{k=0}^{N-1}\left(\frac{x(k)-\mu_x}{\sigma_x}\right)\left(\frac{x_r(k)-\mu_{xr}}{\sigma_{xr}}\right) \tag{6}$$

where μ_x and σ_x are the mean and standard deviation of $x(k)$, respectively, and μ_{xr} and σ_{xr} are mean and standard deviation of $x_r(k)$. The range r is between -1 and 1, and the larger the value, the better quality of the signal.

(e) Percentage-Root-Mean-Square Difference (PRD) calculates the percentage of overall distortion in the signal after denoising. A lower PRD indicates a denoised signal with higher quality.

$$PRD = \sqrt{\frac{\sum_{k=0}^{N-1}(x(k)-x_r(k))^2}{\sum_{k=0}^{N-1}(x(k))^2}} \tag{7}$$

The PRD indicates the distortion in denoised ECG signal. A lower PRD represents better recovery performance.

3. Discrete Wavelet Transform (DWT)

The wavelet transform is an effective method for reducing noise and compressing signals. It provides time-frequency analysis and is useful for biomedical signal processing [30]. With a comparatively fast computing time, the discrete wavelet transform (DWT) constructs multi-resolution analysis using filter banks. There are two different kinds of filters in DWT: low-pass filter $h_0(n)$ and high-pass filter $h_1(n)$, each of length N. Filtering and down-sampling are combined in wavelet analysis. It reduces the signal's sample size by a factor of two. The discrete wavelet transform (DWT) is usually computed using the pyramidal algorithm proposed by Mallat [31]. The schematic of three levels ($J = 3$) decomposition reconstruction DWT is shown in Fig. 3. The pyramidal algorithm is based on a pair of analysis filters, low-pass $h_0(n)$ and high-pass $h_1(n)$, and a pair of synthesis filters, low-pass $g_0(n)$ and high-pass $g_1(n)$. In the z domain, the analysis and synthesis filters are denoted correspondingly as $H_0(z)$, $H_1(z)$, $G_0(z)$, and $G_1(z)$.

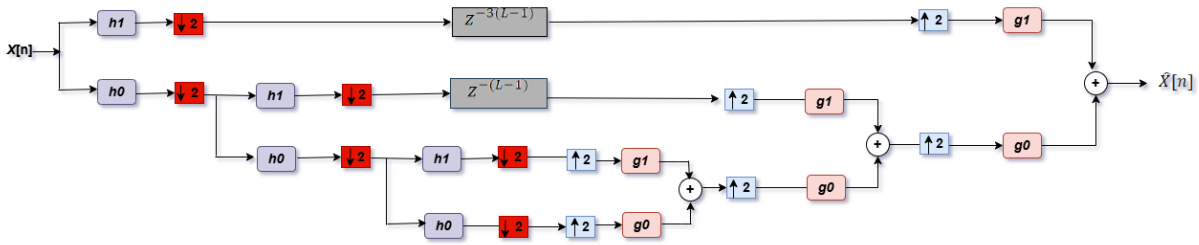

Figure 3. Three-level decomposition reconstruction DWT

The decomposition output at level j of the high-pass analysis filter (detail coefficients) $d_j(n)$ is obtained by filtering the approximation coefficients from the previous level $a_{j-1}(n)$ and downsampling by 2:

$$d_j(n) = \big(h_1(n) * a_{j-1}(n)\big) \downarrow 2 = \sum_{k=0}^{N-1} h_1(2n-k)\, a_{j-1}(k). \tag{8}$$

Similarly, the output of the low-pass analysis filter (approximation coefficients) $a_j(n)$ is:

$$a_j(n) = \big(h_0(n) * a_{j-1}(n)\big) \downarrow 2 = \sum_{k=0}^{N-1} h_0(2n-k)\, a_{j-1}(k). \tag{9}$$

To reconstruct the approximation coefficients $a_{j-1}(n)$ from $d_j(n)$ and $a_j(n)$, the synthesis filters $g_1(n)$ and $g_0(n)$ are used as:

$$a_{j-1}(n) = \sum_k \Big(g_1(n-2k)\, d_j(k) + g_0(n-2k)\, a_j(k)\Big). \tag{10}$$

Each stage of the discrete wavelet transform halves both the number of samples and the effective frequency range until the desired level is reached. The original signal can be reconstructed by combining the coefficients at the final level through the synthesis filter bank. According to Fig. 3, the signals $a_3(n)$ $d_3(n)$ are upsampled by 2 and passed through $g_0(n)$ $g_1(n)$ to produce an intermediate signal $a_2^r(n)$. At the next level, it $d_2(n)$ is delayed by $N-1$ samples and then, together with $a_2^r(n)$, is upsampled by 2 and filtered by $g_0(n)$ and $g_1(n)$ to obtain $a_1^r(n)$. This process continues until the final reconstructed output $a_0^r(n)$ is obtained. The normalized delay unit at each level in a tandem DWT filter bank is defined as [32, 33]:

$$D_j = \big(2^{J-j} - 1\big)(N-1). \tag{11}$$

The analysis stage splits the wavelet filter bank spectrum into two octave bands at each decomposition level. If f_s denotes the sampling frequency, then at level j the approximation and detail subbands occupy $[0,\ f_s/2^{j+1}]$ and $[f_s/2^{j+1},\ f_s/2^j]$, respectively [34, 35, 36]. The equivalent representation used for analysis is shown in Fig. 4 [37, 38, 39]. Using noble identities, the equivalent filters after j decomposition stages for the basic analysis filter bank $H_0(z)$ $H_1(z)$ can be expressed as:

$$A_j(z) = \prod_{k=0}^{j-1} H_0\Big(z^{2^k}\Big). \tag{12}$$

$$D_j(z) = \begin{cases} H_1(z), & j = 1, \\ H_1\Big(z^{2^{j-1}}\Big) \displaystyle\prod_{k=0}^{j-2} H_0\Big(z^{2^k}\Big), & j = 2, 3, \ldots \end{cases} \tag{13}$$

The above equations can be used to compute of equivalent low and high-pass filters after stage j reconstruction using a basic synthesis filter bank $G_0(z)$ and $G_1(z)$ structure. Apply (12) and (13); the decomposition equivalent filters are

$$D_1(z) = H_1(z),\ D_2(z) = H_0(z)H_1(z^2),\ D_3(z) = H_0(z)H_0(z^2)H_1(z^4),\ A_3(z) = H_0(z)H_0(z^2)H_0(z^4)$$

While reconstruction equivalent filters are

$$R_1(z) = G_1(z),\ R_2(z) = G_0(z)G_1(z^2),\ R_3(z) = G_0(z)G_0(z^2)G_1(z^4),\ B_3(z) = G_0(z)G_0(z^2)G_0(z^4)$$

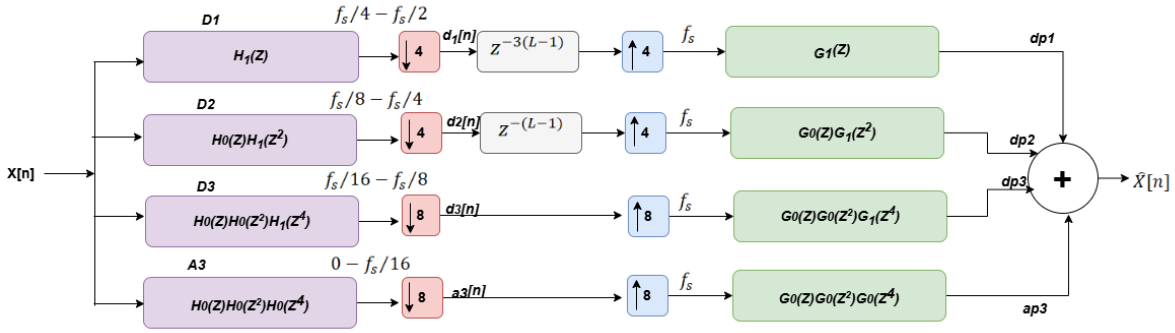

Figure 4. Equivalent representation of the analysis and synthesis octave filter bank for three decomposition levels.

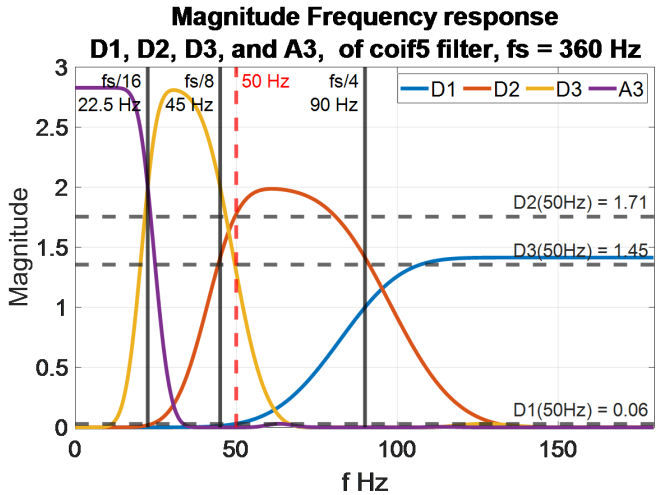

Figure 5. Magnitude frequency response ($f_s = 360$ Hz) of the equivalent analysis octave filter bank using the Coif5 wavelet for three decomposition levels. Note that at $f_p = 50$ Hz, $D_1(f_p) = 0.06$, $D_2(f_p) = 1.71$, $D_3(f_p) = 1.45$, and $A_3(f_p) = 0$.

Figure 5 shows that the frequency response of the analysis filters isn't perfect the frequency intervals don't change sharply. Instead, the filters' magnitude decreases slowly, leveling off to a constant. This means energy leakage changes the frequency distribution within each DWT sub-band. Approximation coefficients show a tendency to scatter at higher levels $f_s/2^{(j+1)}$. On the other hand, detail coefficients are lower than $f_s/2^{(j+1)}$ frequencies and higher than $f_s/2^j$. Hence, there is a band overlap. Therefore, DWT frequency behavior impacts the decomposition level and the wavelet function choices.

4. The material and methodology

To ensure reliable wavelet-based processing, all ECG signals were normalized to the amplitude range of [-1 to +1] and preprocessed using a zero-phase 4th-order Butterworth bandpass filter (0.5–40 Hz). This step removes DC drift and high-frequency interference prior to decomposition, thereby preserving the diagnostic content of the ECG waveform.
In this paper, the comprehensive architecture is designed for the purpose of reducing noise from ECG signals through the using of the DWT. The DWT are used to analyze ECG signal at different resolution levels. The selection of appropriate wavelet basis and the number of decomposition levels are determined by using noise analysis, which effectively separates the signal from the noise. This effectively eliminates noise across frequency bands while ensuring the preservation of important signal characteristics. The choice of the mother wavelet determines the

type of analysis and synthesis filters used in the noise removal process. For efficient operation, the chosen mother wavelet should be similar to the measured ECG signal as accurately as feasible. Also, the extent of discrete wavelet transform (DWT) decomposition influences signal denoising. With too little decomposition, signal-to-noise ratio (SNR) gains are limited. With too much, computation increases and noise reduction could be compromised [40]. The methodology of eliminating each type of noise is separately described.

4.1. Architectural Overview

To enhance clarity and support reader understanding, this subsection provides a high-level overview of the proposed denoising architecture before presenting the detailed mathematical formulation. The proposed framework targets major ECG noise sources separately, depending on the frequency region in which each noise component predominantly appears. Low-frequency variations such as baseline wander are removed from the approximation coefficients. Power-line interference (50 Hz), which is mainly concentrated in the second detail subband, is suppressed through selective filtering. Meanwhile, high-frequency disturbances caused by Gaussian noise are attenuated using soft thresholding applied to the highest detail subband.

Algorithm: Complete Wavelet-Based ECG Denoising Pipeline

Input: Clean ECG $x[n]$, sampling rate f_s; SNR levels $\{-5, 0, 5, 10\}$; selected wavelet function wv (coif3, coif5, sym8, bior6.8); noise model parameters.
Output: Final denoised ECG signals $y_r[n]$ and evaluation metrics.

1. **Preprocessing:** Load ECG, apply 0.5–40 Hz bandpass filter, and select N samples.
2. **Noise generation:** Create AWGN, 50 Hz interference, and baseline wander; combine them to form $n[n]$.
3. **For each SNR level** SNR_i**:**
   (a) Compute scaling factor:
   $$G = \sqrt{\left(\frac{P_x}{P_n}\right) 10^{-SNR_i/10}}$$
   (b) Generate noisy ECG:
   $$y[n] = x[n] + G \cdot n[n]$$
4. **Wavelet decomposition:** Apply 3-level DWT to obtain a_3, d_3, d_2, d_1.
5. **Subband filtering (proposed):**
   (a) $d_2' = d_2 * h_0$
   (b) $d_3' = (d_3 * g_0) * g_1$
6. **Thresholding and reconstruction:** Apply soft thresholding and IDWT to obtain $XD[n]$.
7. **Baseline wander removal:** Perform 8-level DWT and compute
   $$y_r[n] = XD[n] - ap_8[n]$$
8. **Evaluation:** Compute SNR, MSE, PRD, and CC.

Figure 6. Complete pseudocode of the proposed wavelet-based ECG denoising pipeline.

A three-level DWT decomposition is used to divide the ECG into well-defined frequency bands, enabling more accurate noise reduction compared to uniformly processing all wavelet coefficients. With this frequency-specific strategy, important diagnostic characteristics such as QRS slopes, P-wave morphology, and the ST-segment are preserved while noise is effectively suppressed. Fig. 3 provides a conceptual illustration of this processing flow prior to the mathematical development. To ensure full reproducibility of the proposed denoising architecture, the analysis and synthesis filter coefficients were obtained directly from the MATLAB Wavelet Toolbox. The following function was used to extract the corresponding filter banks for each mother wavelet evaluated in this work:

colback=blue!10, colframe=white, boxrule=0pt, left=6pt,right=6pt,top=6pt,bottom=6pt]

```
h0, h1, g0, g1 = wfilters('bior6.8');
```

The same MATLAB function was used for alternative wavelets, including coif5 and sym8. All simulations and experiments were conducted in MATLAB R2021b with Wavelet Toolbox Version 5.4, ensuring that the filter responses, subband structures, and reconstruction performance reported in this paper can be reproduced accurately in independent setups.

4.2. New proposed method to weaken the 50 Hz power line interference

A new method is suggested in this paper to weaken the 50 Hz power line interference. To explain this method, refer to Fig. 4 of the equivalent representation of the sym8 analysis filters; the spectrum magnitudes at $f_p = 50$ Hz are $D_1(f_p) = 0.06$, $D_2(f_p) = 1.7137$ and $D_3(f_p) = 1.4533$, respectively. It is apparent that 50 Hz power line interference occurs mostly in DWT Bands D_2 and D_3. To reject the 50 Hz power line, the analysis low-pass filter $h_0(k)$ filtering is connected after the details output d_2. Additionally, in cascade, the reconstruction low-pass filter $g_0(k)$ and high-pass filter $g_1(k)$ are connected after d_3 output as shown in Fig. 7.

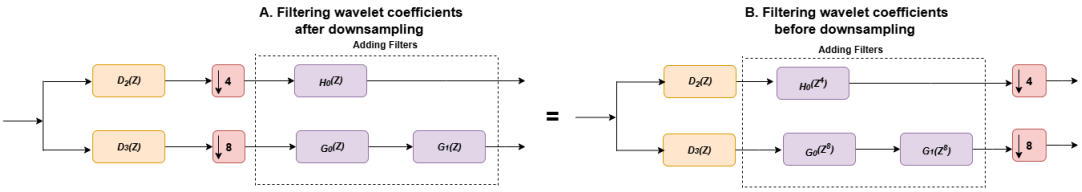

Figure 7. Equivalent representation of analysis octave filter bank of $D_2(z)$ and $D_3(z)$ after connecting $H_0(z)$ after d_2 and $G_0(z)G_1(z)$ after d_3. Correspondingly, the equivalent analysis octave filter becomes $D_2(z)H_0(z^4)$ and $D_3(z)G_0(z^8)G_1(z^8)$ respectively.

Moreover, to enhance selective noise suppression for each frequency band, modifications were applied to the standard wavelet filter-bank structure. Wavelet subbands are affected by different noise; baseline wander mostly modifies the low-frequency approximation. Power line noise is mostly in the d2 and d3 bands. The Gaussian noise is spread across all the subbands and remains as Gaussian noise, with most noise information residing in the high-frequency detail d1 subband. Therefore, level 1 subband d1 detail coefficients capture the majority of the noise.

This makes the d1 subband the most common groundwork for estimating the Gaussian noise standard deviation [32]. Wavelet thresholding is a good denoising estimator where coefficients below a certain threshold are set to zero (hard thresholding) or shrunk towards zero (soft thresholding). The standard DWT noise reduction uses the same threshold for each subband. The universal threshold is used, which is based on the Gaussian noise standard deviation estimated from subband d1 detail coefficients.

The proposed method is used to eliminate power line noise in the d2 and d3 bands before applying wavelet thresholding in a specific manner. It uses H_0 after the d2 subband to more efficiently eliminate 50 Hz interference. Then, a series of G_0 and G_1 comes after the d3 subband to eliminate 50 Hz interference. Then applying wavelet thresholding efficiently reduces Gaussian noise but does not smooth the QRS complex slopes too much. The study adopted this modification after observing that it provides better SNR and lower PRD than the traditional approach, while preserving the ST-segment and T-wave appearance as normal.

To illustrate this idea, the equivalent representation in Fig. 4 is used. From the equivalent representation, the magnitude frequency responses are shown in Fig. 8(a) and Fig. 8(b) for the Sym8 wavelet at sampling frequency $f_s = 360$ Hz for $D_2(z)H_0(z^4)$ and $D_3(z)G_0(z^8)G_1(z^8)$, respectively, to eliminate 50 Hz interference.

The performance of the improved SNR when employing various wavelet filters for three levels of DWT decomposition using the proposed method is illustrated in Fig. 9. It is obvious that enhancement is better at low SNR_{in}. The improvement becomes less as SNR_{in} is increased. The best filter is coif5.

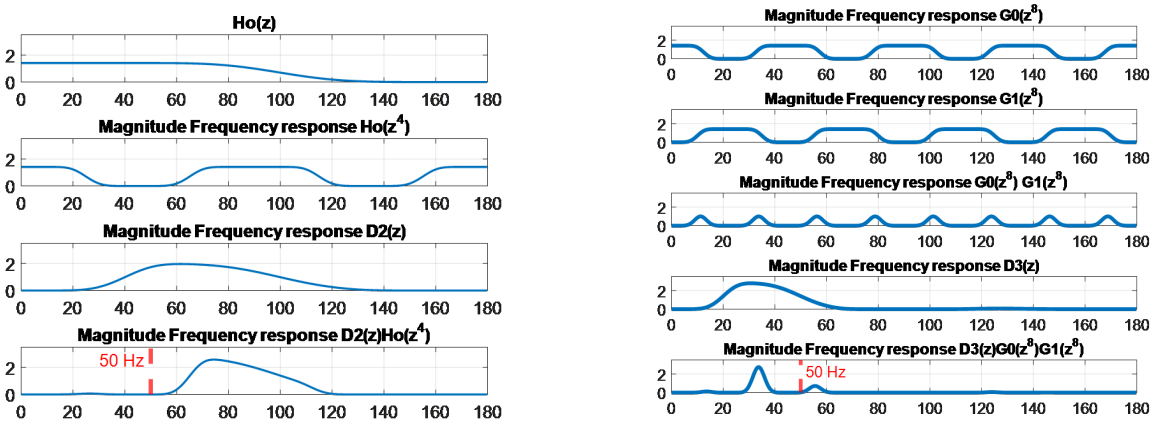

(a) (b)

Figure 8. The magnitude frequency response for the Sym8 wavelet at sampling frequency $f_s = 360$ Hz for (a) $D_2(z)H_0(z^4)$ and (b) $D_3(z)G_0(z^8)G_1(z^8)$.

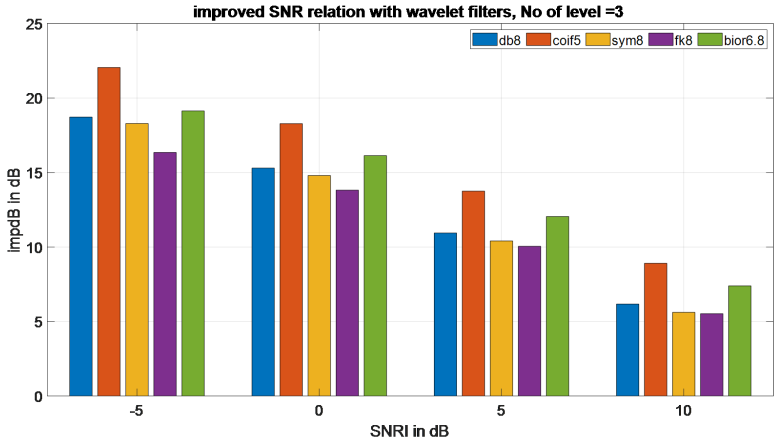

Figure 9. Performance of the improved SNR when employing various wavelet filters for 3 level of DWT decomposition using hard thresholding method

The qualitative results by adding 50 Hz power line to the clean simulated synthetic ECG at different input SNR levels (-5 dB, 0 dB, 5 dB, and 10 dB) at level 3 of DWT decomposition for the coif5 filter are shown in Fig. 10.

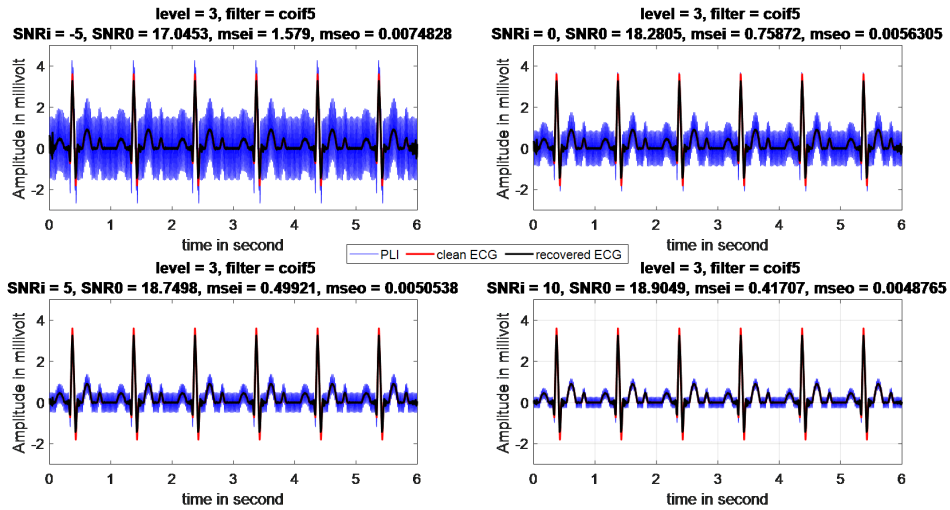

Figure 10. The corrupted signals by adding a 50 Hz power line to clean simulated synthetic ECGs of different input SNR levels (-5 dB, 0 dB, 5 dB, and 10 dB) at level 3 of DWT decomposition for coif5 filter.

4.3. Analysis of denoising ECG using DWT

To reduce the effect of additive white Gaussian noise (AWGN), a threshold technique is applied. The wavelet denoising by the thresholding procedure is processed in three steps [41, 42, 43, 44]. The first step is signal decomposition, using a suitable wavelet filter family $h_o(n)$ and $h_1(n)$. Thresholding of the DWT details coefficients d_j represent the second step in this process. Commonly, there are two thresholding methods, named, hard and soft thresholding. The two thresholding methods can be expressed mathematically as

$$dt_j(\text{Hard threshold}) = \begin{cases} d_j, & \text{if } |d_j| > Th_j \\ 0, & \text{if } |d_j| \leq Th_j \end{cases} \tag{14}$$

$$dt_j(\text{Soft threshold}) = \begin{cases} \text{sign}(d_j)(|d_j| - Th_j), & \text{if } |d_j| > Th_j \\ 0, & \text{if } |d_j| \leq Th_j \end{cases} \tag{15}$$

The coefficients dt_j and d_j are wavelet coefficients after and before thresholding.

Soft thresholding reduces coefficients below a predetermined threshold to zero while compressing the others toward zero. This gives a smoother, cleaner signal by reducing the smaller coefficients. Hard thresholding also zeroes out coefficients below a certain level, but it leaves the rest unmodified. Therefore, it produces a cleaner signal that's more sparse and has sharper changes. The global threshold selection approach is used in this paper. Estimate the noise standard deviation using the robust median estimator formula $\sigma_e = \text{median}(|d_1|)/0.6457$. Then compute the universal threshold $Thr = \sigma_e\sqrt{2\ln(N_{d_1})}$ where N_{d_1} the length is d_1 [45, 46, 47]. The SNR_i and SNR_o are measured for both hard and soft thresholding for wavelet filter coif5 as shown in Fig. 11 for decomposition level from 1 to 8. They SNR_i are selected in the range of -5 dB to 15 dB, by steps of 5 dB. It is clear that for low values of SNR_I, both thresholds give better imp_{dB} results at lower DWT levels. The decomposition level 3 gives the best results for hard and soft thresholding. The three levels are selected using a soft threshold, which has a better denoising performance than hard threshold.

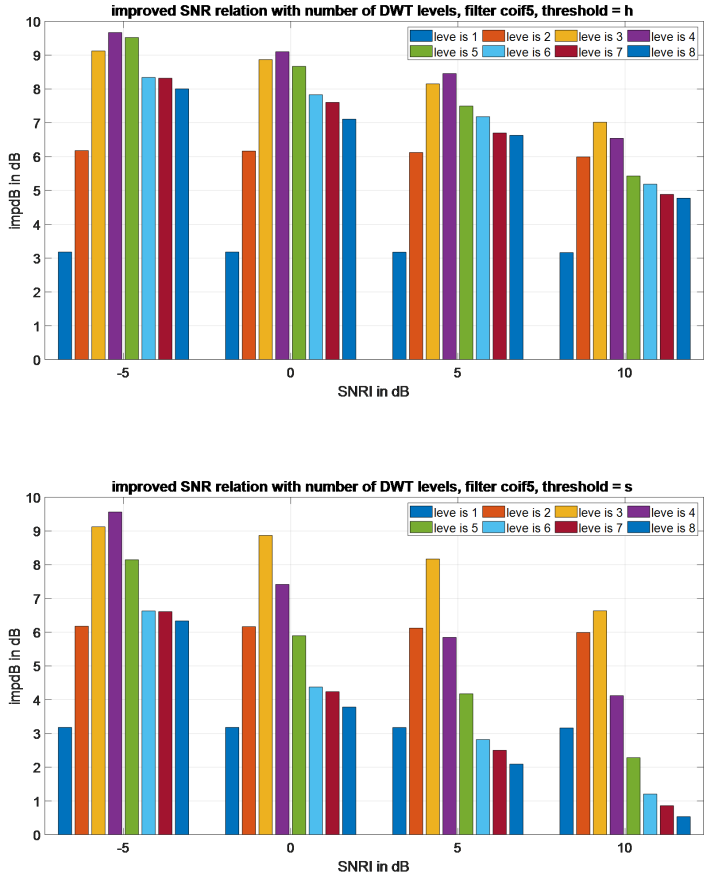

Figure 11. Improved SNR relation with the number of DWT levels using coif5 filter for (a) hard thresholding and (b) soft thresholding.

The performance of the improved SNR when employing various wavelet filters at three levels of DWT decomposition using soft thresholding method is illustrated in Fig. 12. It is obvious that the coif filter gives best results.

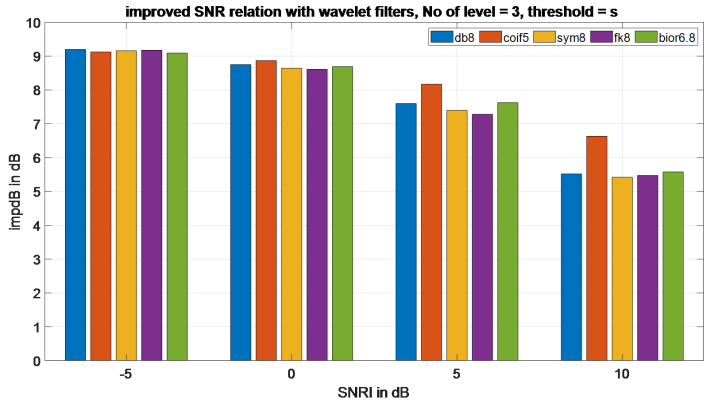

Figure 12. Performance of the improved SNR when employing various wavelet filters at 3 levels of DWT decomposition using the soft thresholding method.

In order to evaluate how well the wavelet denoising works, corrupted ECG signals were processed. These signals, with varying signal-to-noise ratios (-5 dB, 0 dB, 5 dB, and 10 dB), were created by adding simulated Gaussian white noise to a clean, simulated synthetic ECG signal as shown in Fig. 13. The noisy ECG signal is denoised with 3 levels of DWT decomposition for coif5 using the soft threshold method. It can be observed that a valuable amount of noise has been removed. At 5 dB, cases of massive noise is suppressed, and the outlook frame of the clean ECG is recovered. In light of the 10 dB cases the feature of clean ECG is entirely recovered with only slightly harmed since the soft thresholding method is satisfactory.

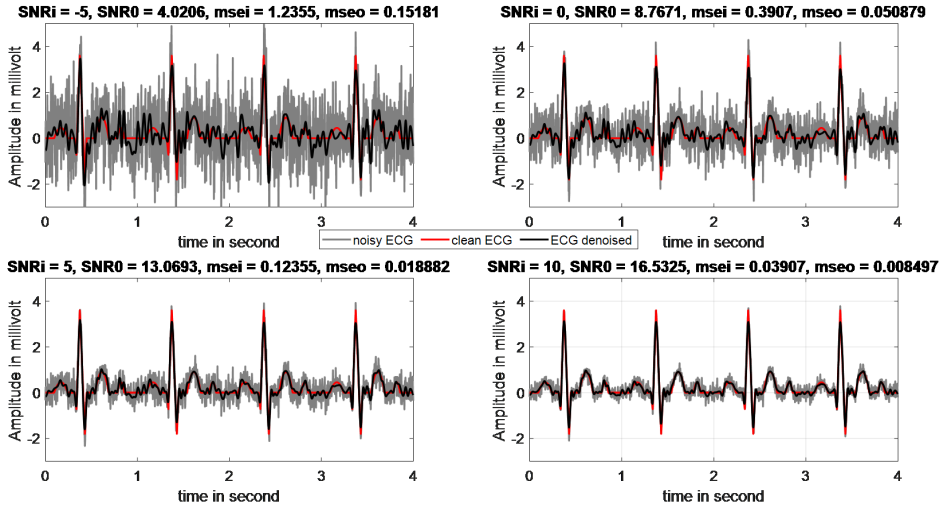

Figure 13. The noisy ECG signal is denoised with 3 levels of DWT decomposition for coif5 filter using the soft threshold method. The SNRi are -5 dB (upper left), 0 dB (upper right), 5 dB (lower left), and 10 dB (lower right)

4.4. Remove of wander noise

Baseline wandering is a particular kind of noise that introduces a low-frequency distortion onto the ECG signal. Variations in the resistance between the electrode and the patient's skin are the cause of this noise. According to [45], baseline wandering typically occurs in a frequency band below 1 Hz. In this work, the DWT decomposition is applied to the noisy ECG till 8 levels. At any level j of decomposition,$1 \leq j \leq 8$, the ideal frequency range of approximation coefficients a_j is $[0 - f_s/2^{j+1}]$. On the other hand, detail coefficients D_j are $[f_s/2^{j+1} - f_s/2^j]$. Table 2 lists the optimal frequency range for each level. The results suggest baseline wandering appears in A_8, given that it is a low-frequency activity within the $0 - 0.7031$ Hz range.
To remove baseline wander from ECG signal using DWT, 8 decimators can be implemented using multistage decomposition low pass filter $h_0(n)$ followed by downsampling by 2 as cascade decimators as shown in Fig. 14.a. In the same manner, the 8 interpolators can be implemented using multistage reconstruct up sampling 2 flowed by low pass filter $g_0(n)$ in cascade as depicted in Fig. 14.b. The single stage equivalence for the multistage structure for 8 decimators and interpolators are shown in Fig 14.c and Fig 14.d respectively. The bior6.8 wavelet was selected for this stage, with filter length $N = 18$ for both the analysis filter $h_0(n)$ and the synthesis filter $g_0(n)$, as it provided strong low-frequency separation and optimal PRD performance among the tested wavelets.

Table 2. Analysis of the octave filter for the 8-level DWT decomposition at $f_s = 360$ Hz.

Level j	**Analysis octave filter**	**Ideal Frequency Range (Hz)**
1	D1	90 – 180
2	D2	45 – 90
3	D3	22.5 – 45
4	D4	11.25 – 22.5
5	D5	5.6 – 11.25
6	D6	2.8 – 5.6
7	D7	1.4 – 2.8
8	D8	0.7031 – 1.4062
8	A8	0 – 0.7031

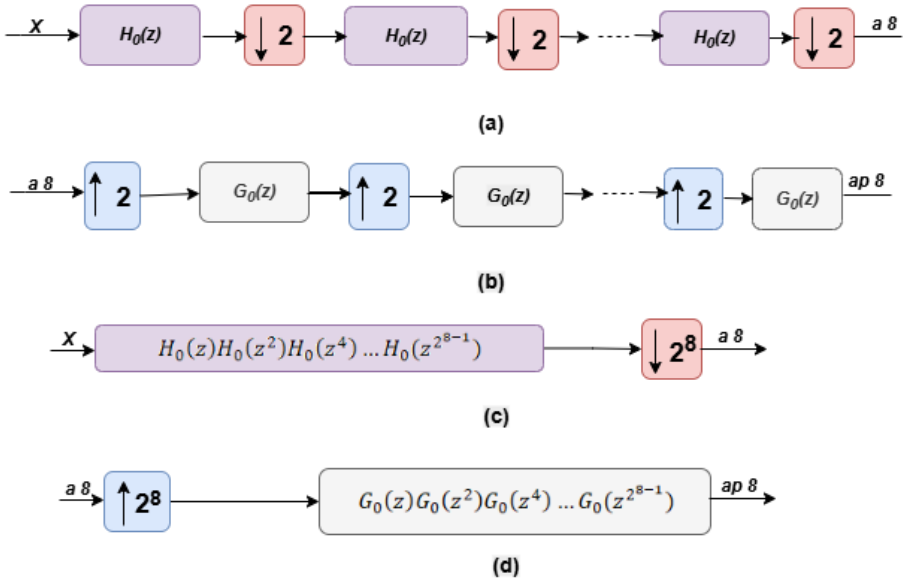

Figure 14. Implementation of cascade decimators and interpolators: (a) multistage decimator input x and output a8 (b) multistage interpolator input a8 and output ap8 (c) equivalence for multistage structure decimator; (d) equivalence for multistage structure interpolator

The performance of the wavelet method is evaluated by removing baseline wandering from the ECG signal. The contaminated power line interference with ECG signals at different input SNR levels (-5 dB, 0 dB, 5 dB and 10 dB) are generated. The result removed with 8 levels of DWT decomposition for different type of wavelet filters to remove baseline wandering is shown in Fig. 15. It is obvious that bior6.8 filters give the best results.

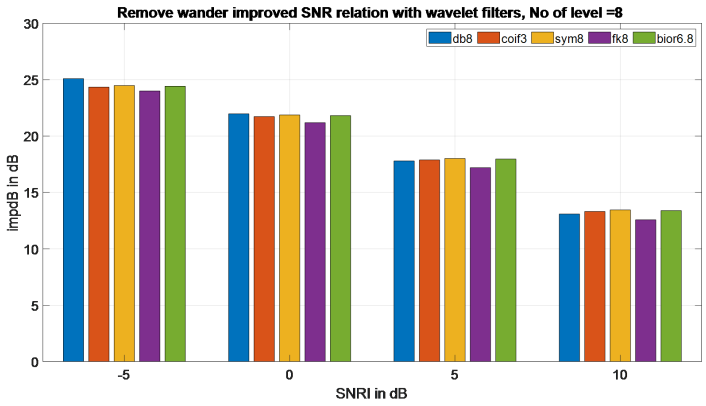

Figure 15. performance of the improved SNR when employing various wavelet filters at 8 level of DWT decomposition to remove 50 Hz power line interference

The qualitative results by adding baseline wander to the clean simulated synthetic ECG at different input SNR levels (-5 dB, 0 dB, 5 dB and 10 dB) at level 8 of DWT decomposition for coif5 filter are shown in Fig. 16.

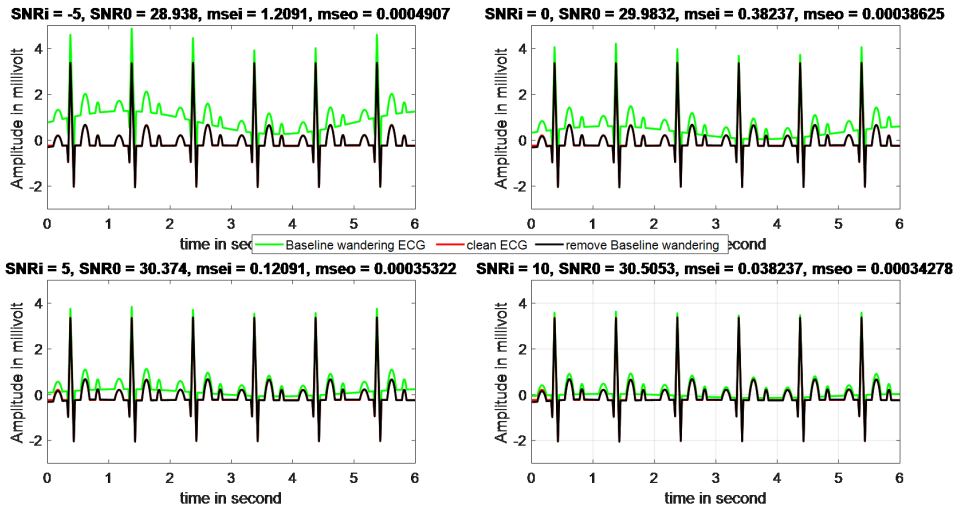

Figure 16. The baseline wandering ECG signal is removed at 8 levels of DWT decomposition for coif5 filter. The SNRi are -5 dB (upper left), 0 dB (upper right), 5 dB (lower left), and 10 dB (lower right).

4.5. Proposed architecture

After analyzing the results in the previous section, the architecture shown in Fig. 17 is proposed. The proposed architecture eliminates the 50 Hz power line and Gaussian noises using three levels analysis/synthesis DWT. To decrease the effect of the 50 Hz power line the analysis low-pass filter $H_0(z)$ is connected after the detail output, D_j while after D_j the output, the synthesis low-pass filter $G_0(z)$ and high-pass filter $G_1(z)$ are connected in cascade. To reduce the effect of additive white Gaussian noise (AWGN), threshold techniques are applied on the three levels of DWT using soft threshold function. To detect the baseline wander from an noisy ECG signal using DWT, 8 multistage decimators of low-pass filter $h_0(n)$ flowed by downsampling by 2 are connected in cascade. In the same manner, the 8 multistage interpolators of upsampling 2 followed by a low-pass filter $g_0(n)$ are connected in cascade.

To avoid length mismatch during reconstruction, all additional filtering operations are implemented using the same boundary extension rule (`dwtmode('per')`) that ensures periodic symmetric padding and consistent support across all decomposition levels. The filtered d_2 and d_3 detailed coefficients are kept identical in length to their originals using convolution with 'same' mode, preventing any misalignment during synthesis. The intrinsic delay differences introduced by the parallel branches are compensated through the standard DWT shift alignment defined in $D_j = (2^{J-j} - 1)(N - 1)$, which preserves temporal consistency of the reconstructed signal. For the baseline wander removal branch, the 8-stage decimator/interpolator chain was implemented directly using cascaded low-pass filters and dyadic down/upsampling, rather than collapsing the structure into a single high-order equivalent filter. This preserves numerical stability and reduces computational cost while maintaining the theoretical filtering response described in Section 3.

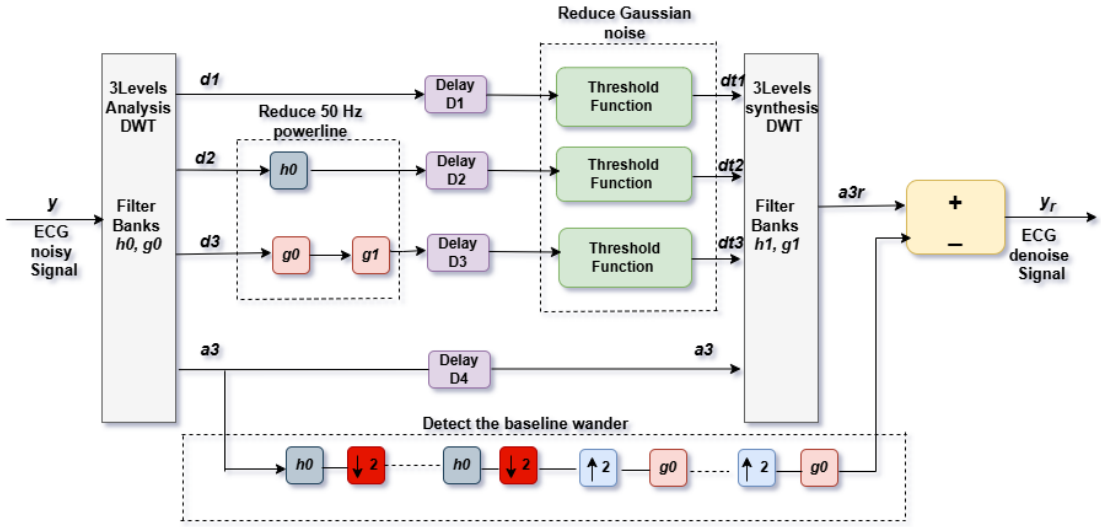

Figure 17. The proposed architecture eliminates all types of noise contaminating ECG signals

5. Experimental results and Discussion

5.1. Evaluation Under Synthetic Noise Conditions

The performance results of eliminate all types of noise contaminating ECG signals together using the proposed architecture. The corrupted ECG $y(k)$ is obtained by mixing a clean synthetic ECG with noise types. The kinds of noises carried out in this study are a white Gaussian noise, the baseline wander line drift, and the power line interference. Corrupted signal is expressed in the following form:

$$y(k) = x(k) + ng(k) + pl(k) + wd(k) \tag{16}$$

where, $x(k)$ represents the clean ECG signal, $ng(k)$ additive white Gaussian noise (AWGN), $pl(k)$ 50 Hz power line, and $wd(k)$ baseline wander, and their parameters are presented on the Table 3. The average power of the clean ECG signal $x(k)$ is denoted as P_x.

The mathematical model of $ng(k)$ additive white Gaussian noise (AWGN) is

$$ng(k) = \sigma rg(k) \tag{16.1}$$

$rg(n)$ is normalized white Gaussian noise with zero mean and unit variance $N(0, 1)$. The σ is desired standard deviation is $ng(k)$, thus the variance of $ng(k)$ is σ^2. Therefore, the average power of $n(k)$ is $P_{ng} = \sigma^2$.

The $pl(k)$ 50 Hz power line is

$$pl(k) = A_{50} \sin(2\pi k f_p / f_s) \tag{16.2}$$

where A_{50} is amplitude and $f_p = 50$ Hz is the interference frequency. The standard deviation $pl(k)$ is $A_{50}/\sqrt{2}$ with variance $A_{50}^2/2$. Therefore, the average power of $p(k)$ is $P_{pl} = A_{50}^2/2$.

The mathematical model of baseline wander $w(k)$ is

$$wd(k) = DC + A_w \sin(2\pi k f_w/f_s) \tag{16.3}$$

where DC is the wander mean offset drift, the A_w is the AC amplitude, and f_w is wander frequency. The average power of $w(k)$ is $P_{wd} = DC^2 + A_w^2/2$.

The denoised signal output of the proposed architecture is denoted as $y_r(k)$.

Table 3. Parameter values used in the synthetic noise models.

Noise type	**Equation**	**Parameter**	**Symbol**	**Value**
Additive white Gaussian noise	(16.1)	Standard deviation	σ	2
50 Hz power-line interference	(16.2)	Amplitude	A_{50}	4
		Interference frequency	f_{50}	50
Baseline wander	(16.3)	DC offset	D_C	20
		AC amplitude	A_w	10
		Wander frequency	f_w	0.1
Common parameter	–	Sampling frequency	f_s	360

These noise models were applied to generate the corrupted ECG signal used as input to the proposed denoising architecture. After applying the complete denoising pipeline, the computational efficiency of the algorithm was also evaluated. Using MATLAB's built-in `tic`/`toc` functions, the complete denoising pipeline (including noise generation, SNR scaling, 3-level DWT decomposition, subband filtering, thresholding, and wander removal) required 2.26 seconds to process a single 4096-sample ECG segment, which corresponds to $4096/360 = 11.38$ seconds of ECG. By linear extrapolation, a full 30-minute MIT-BIH record (around 158 segments) would require approximately 6 minutes, demonstrating the computational efficiency of the proposed denoising pipeline. All experiments were performed on a standard computing platform (Intel Core i7, 16 GB RAM, MATLAB R2021b).

To investigate the effectiveness of thresholding types, the proposed architecture was first evaluated using the *coif3* wavelet with both hard and soft thresholding functions.
A global soft-thresholding strategy was consistently applied in all experiments, using the universal 'sqtwolog' rule with SCAL='sln', uniformly across all three DWT levels of the proposed architecture.
The results are summarized for the real ECG signal from MIT-BIH Normal Sinus Rhythm Database [47] in this paper; this signal is named as `ECG127_360`. It could be observed that soft thresholding consistently outperformed hard thresholding, achieving higher SNR improvement (up to 3.596 dB vs. 3.495 dB), stronger correlation coefficients (0.9779 vs. 0.9773), and lower percentage root mean square difference (PRD) values. These results confirm that soft thresholding better preserve ECG morphology while successfully reducing noise from ECG signals as shown in the Table 4(a) and Table 4(b). To ensure statistical reliability and reproducibility of the reported results, all experiments were repeated over multiple independent noise realizations. For each input SNR level (-5, 0, 5, and 10 dB), 10 different random noise sequences were generated for AWGN, baseline wander, and 50 Hz interference. The proposed denoising pipeline was applied to each noisy realization, and performance metrics (SNR, MSE, PRD, and CC) were computed separately.

For each metric, the mean (μ) and standard deviation (σ) were calculated as:

$$\mu = \frac{1}{R}\sum_{r=1}^{R} M_r, \qquad \sigma = \sqrt{\frac{1}{R-1}\sum_{r=1}^{R}(M_r - \mu)^2}. \tag{17}$$

where M_r represents the metric value for the r-th trial and $R = 10$ is the total number of trials. To assess whether improvements achieved by the proposed method are statistically significant compared to baseline methods, paired t-tests were conducted at a significance level of $\alpha = 0.05$.

Table 4(a): Performance of proposed architecture using hard thresholding (Coif5 wavelet).

SNRi (dB)	SNRo (dB)	SNRimp (dB)	MSE_i	MSE_o	CC	PRD (%)
-5	13.03 ± 0.32	18.03 ± 0.28	0.9636 ± 0.012	0.01516 ± 0.0011	0.97483 ± 0.0021	22.30 ± 0.95
0	13.46 ± 0.29	13.46 ± 0.24	0.3047 ± 0.009	0.01375 ± 0.0009	0.97718 ± 0.0019	21.24 ± 0.88
5	13.45 ± 0.26	8.45 ± 0.21	0.09636 ± 0.006	0.01377 ± 0.0008	0.97715 ± 0.0018	21.26 ± 0.84
10	13.50 ± 0.23	3.50 ± 0.17	0.03047 ± 0.003	0.01362 ± 0.0007	0.97739 ± 0.0016	21.14 ± 0.80

Table 4(b): Performance of proposed architecture using soft thresholding (Coif3 wavelet).

SNRi (dB)	SNRo (dB)	SNRimp (dB)	MSE_i	MSE_o	CC	PRD (%)
-5	13.03 ± 0.32	18.03 ± 0.28	0.9636 ± 0.012	0.01516 ± 0.0011	0.97483 ± 0.0021	22.30 ± 0.95
0	13.45 ± 0.29	13.45 ± 0.24	0.3047 ± 0.009	0.01376 ± 0.0009	0.97717 ± 0.0019	21.25 ± 0.87
5	13.58 ± 0.27	8.58 ± 0.22	0.09636 ± 0.006	0.01337 ± 0.0008	0.97782 ± 0.0017	20.95 ± 0.83
10	13.60 ± 0.24	3.60 ± 0.18	0.03047 ± 0.003	0.01331 ± 0.0007	0.97791 ± 0.0016	20.90 ± 0.80

The performance of the proposed architecture with sym8, coif5, and bior6.8 wavelets under soft thresholding is presented in Tables 5(a), 5(b), and 5(c). The sym8 wavelet performed the highest correlation coefficients, around 0.991 across all noise levels, indicating the strong similarity between the denoised and clean ECG signals; however, its relatively higher PRD values around 13 to 15% suggest that some residual distortion remained in the reconstructed ECG signal. The coif5 wavelet showed stable and balanced performances, with CC values around 0.975 and consistent SNR improvements across all SNR levels, making it a robust option despite slightly higher PRD values around 21 to 23%. In contrast, the bior6.8 wavelet provided the best overall performance, achieving high correlation coefficients (up to 0.986) together with the lowest PRD values around 16 to 18%, consequently offering superior noise suppression while preserving ECG signal morphology.
These findings indicate that while sym8 and coif5 show competitive performance, bior6.8 with soft thresholding appears as the most effective wavelet for ECG denoising on the real `ECG127_360` signal.

Table 5(a): Performance of proposed architecture using soft thresholding (sym8 wavelet).

SNRi (dB)	SNRo (dB)	SNRimp (dB)	MSE_i	MSE_o	CC	PRD (%)
-5	16.48 ± 0.42	21.48 ± 0.35	1.2005 ± 0.018	0.00854 ± 0.0009	0.9887 ± 0.0012	15.00 ± 0.88
0	17.25 ± 0.39	17.25 ± 0.31	0.3796 ± 0.011	0.00716 ± 0.0008	0.9905 ± 0.0010	13.73 ± 0.80
5	17.53 ± 0.36	12.53 ± 0.28	0.1201 ± 0.007	0.00669 ± 0.0007	0.9912 ± 0.0009	13.28 ± 0.76
10	17.70 ± 0.32	7.70 ± 0.25	0.0379 ± 0.004	0.00644 ± 0.0006	0.9915 ± 0.0008	13.03 ± 0.72

Table 5(b): Performance of proposed architecture using soft thresholding (coif5 wavelet).

SNRi (dB)	SNRo (dB)	SNRimp (dB)	MSE_i	MSE_o	CC	PRD (%)
-5	12.73 ± 0.40	17.73 ± 0.34	0.9636 ± 0.015	0.01625 ± 0.0012	0.9729 ± 0.0020	23.10 ± 1.05
0	13.09 ± 0.37	13.09 ± 0.30	0.3047 ± 0.010	0.01497 ± 0.0010	0.9751 ± 0.0018	22.16 ± 0.95
5	13.20 ± 0.34	8.20 ± 0.27	0.0964 ± 0.006	0.01459 ± 0.0009	0.9776 ± 0.0016	21.88 ± 0.90
10	13.23 ± 0.31	3.23 ± 0.24	0.0305 ± 0.003	0.01450 ± 0.0008	0.9759 ± 0.0015	21.81 ± 0.85

Table 5(c): Performance of proposed architecture using soft thresholding (bior6.8 wavelet).

SNRi (dB)	SNRo (dB)	SNRimp (dB)	MSE_i	MSE_o	CC	PRD (%)
-5	14.67 ± 0.45	19.67 ± 0.37	0.9636 ± 0.015	0.01040 ± 0.0011	0.9828 ± 0.0019	18.47 ± 1.05
0	15.29 ± 0.42	15.29 ± 0.33	0.3047 ± 0.010	0.00901 ± 0.0009	0.9851 ± 0.0017	17.19 ± 0.98
5	15.53 ± 0.39	10.53 ± 0.30	0.0964 ± 0.006	0.00853 ± 0.0008	0.9859 ± 0.0016	16.73 ± 0.92
10	15.52 ± 0.35	5.52 ± 0.27	0.0305 ± 0.003	0.00855 ± 0.0008	0.9859 ± 0.0015	16.75 ± 0.88

The study used the MIT-BIH Arrhythmia database to perform a performance comparison. Signals 100, 103, and 105 were used, each lasting 30 minutes with a sampling rate of 360 Hz. Three types of noise were added: additive white Gaussian noise (AWGN), 50 Hz power-line interference, and baseline wander noise from the MIT-BIH Noise Stress Test Database. The performance of the proposed architecture was evaluated under SNR levels of -5, 0, 5, and 10 dB. Quantitative evaluation was carried out using SNR, RMSE, PRD, and CC. Even at $SNR_i = -5$ dB, correlation coefficients above 0.90 were achieved, confirming robustness under highly noisy conditions.

The study compared *coif5*, *sym8*, and *bior6.8* wavelets at different noise levels to identify the most suitable denoising framework. The *sym8* wavelet achieved the highest correlation (above 0.99) but showed higher PRD values, indicating waveform distortion. The *coif5* wavelet demonstrated stable performance but was not optimal. In contrast, the *bior6.8* wavelet achieved the lowest PRD values (18%) with high correlation (above 0.985), preserving ECG morphology effectively. Therefore, the *bior6.8* wavelet was selected due to its balanced performance.

Table 6. Denoising performance of the proposed architecture on selected MIT-BIH records and synthesized ECG under various noise conditions.

Record	SNRi	SNRo	SNRimp	MSE_i	MSE_o	CC	PRD (%)
Synthesized ECG	-5	16.98 ± 0.42	21.98 ± 0.35	1.2005 ± 0.018	0.00990 ± 0.0009	0.9922 ± 0.0010	14.17 ± 0.88
Synthesized ECG	0	18.07 ± 0.39	18.07 ± 0.31	0.3796 ± 0.011	0.00716 ± 0.0008	0.9922 ± 0.0009	12.48 ± 0.80
Record 100	-5	7.99 ± 0.51	12.99 ± 0.42	0.08685 ± 0.006	0.01733 ± 0.0013	0.9173 ± 0.0024	39.83 ± 1.45
Record 100	0	8.08 ± 0.48	8.08 ± 0.38	0.02746 ± 0.004	0.9189 ± 0.0021	0.9189 ± 0.0021	39.47 ± 1.32
Record 103	-5	16.42 ± 0.46	15.61 ± 0.37	0.08479 ± 0.006	0.9557 ± 0.0019	0.9557 ± 0.0019	29.46 ± 1.12
Record 103	0	10.90 ± 0.43	10.90 ± 0.34	0.02681 ± 0.003	0.9585 ± 0.0017	0.9585 ± 0.0017	28.52 ± 1.05
Record 105	-5	17.16 ± 0.44	22.16 ± 0.36	0.08649 ± 0.006	0.9904 ± 0.0012	0.9904 ± 0.0012	13.88 ± 0.86
Record 105	0	18.79 ± 0.41	18.79 ± 0.32	0.02735 ± 0.003	0.9926 ± 0.0011	0.9926 ± 0.0011	12.13 ± 0.82

5.2. Evaluation on Challenging Real MIT-BIH Arrhythmia Records

To examine the performance of the denoising procedure and its applicability under realistic conditions, the proposed method was evaluated on challenging ECG signals from the MIT-BIH Arrhythmia Database, including records 104, 105, 108, 114, 208, and 228. These recordings contain real artifacts such as baseline wander, muscle noise, electrode motion effects, and morphological variations. No synthetic noise was added; the original signals were used to assess performance under clinical conditions.

Table 7 summarizes the output SNR, MSE, CC, and PRD results. High SNR values (14–20 dB) and strong correlations (CC = 0.98–0.995) were achieved for most records, indicating effective noise suppression with morphology preservation. Record 114 shows degraded performance (CC = 0.9248, PRD = 38%) due to severe motion artifacts, consistent with previous studies.

Table 7. Denoising performance on real MIT-BIH records using bior6.8 wavelet (no synthetic noise).

Record	SNRo (dB)	MSE_o	CC	PRD (%)
104	20.16 ± 0.58	0.00026 ± 0.00004	0.9952 ± 0.0011	9.82 ± 0.74
105	14.42 ± 0.63	0.00085 ± 0.00009	0.9818 ± 0.0016	19.01 ± 1.02
108	15.49 ± 0.55	0.00062 ± 0.00007	0.9860 ± 0.0014	16.81 ± 0.91
114	8.39 ± 0.71	0.00235 ± 0.00018	0.9248 ± 0.0029	38.07 ± 2.11
208	14.34 ± 0.59	0.00191 ± 0.00012	0.9815 ± 0.0018	19.20 ± 1.05
228	14.16 ± 0.61	0.00020 ± 0.00003	0.9806 ± 0.0017	19.59 ± 1.09

To further analyze morphological preservation, a pathological beat from record 208 was examined. As illustrated in Fig. 18, the denoising process effectively removes baseline wander and high-frequency noise while preserving clinically important features such as the QRS complex, ST-segment, and T-wave morphology.

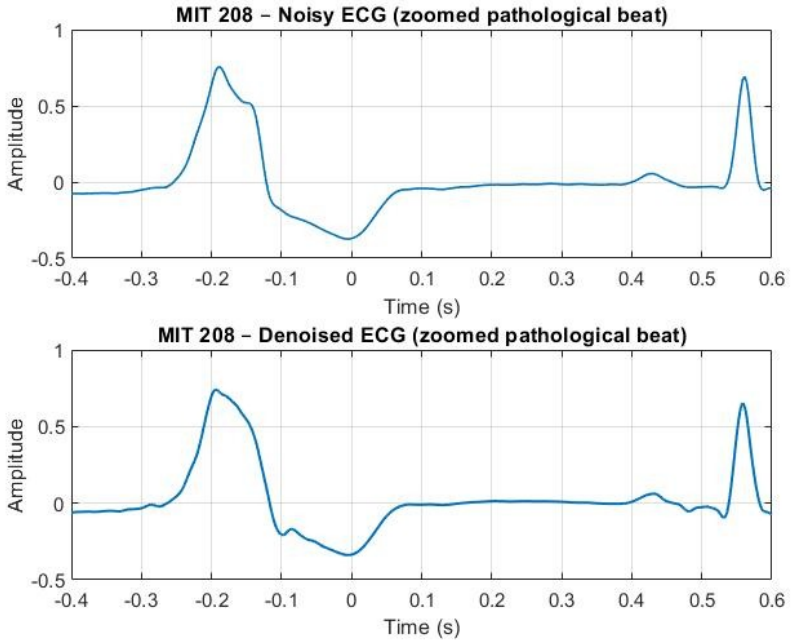

Figure 18. Magnified pathological heartbeat from record 208, demonstrating preservation of QRS and ST-segment after denoising.

5.3. Comparison with Traditional Denoising Methods

Table 8 presents the comparison between the proposed unified DWT-based architecture and traditional filtering methods. Across all noise types, the proposed DWT-based architecture consistently outperformed traditional denoising methods across all tested noise types. For power line interference (50 Hz), it achieved a higher correlation coefficient, greater SNR improvement, and lower MSE compared to the notch filter, which fits with the findings of Martens *et al.* [2] and Der Lin & Hu [10], who also highlighted the limitations of notch-based suppression. For the baseline draft, the DWT approach slightly increased correlation and SNR, with a slight rise in MSE relative to low-pass filter, in agreement with the nonlinear filter bank approaches by Leski & Henzel [8]. Similarly, for white Gaussian noise ($\sigma = 0.3$), the proposed architecture achieved higher correlation, better SNR improvement, and lower MSE than the average filter, confirming observations from Awal *et al.* [1] and Jenkal *et al.* [13] that wavelet thresholding methods provides superior denoising performance.

For deep-learning baselines, two representative recent studies were considered. Antczak proposed a deep recurrent neural network (DRNN) for ECG denoising under mainly additive white Gaussian noise[6], while Rifai et al. developed a 1D convolutional autoencoder evaluated on the MIT-BIH Noise Stress Test Database under baseline wander, muscle artifact, and electrode motion noise [7]. Because these studies used different datasets and noise conditions, their results are reported as published rather than re-implemented.

Table 8. Comparison of traditional filtering methods, recent deep-learning approaches, and the proposed DWT-based architecture.

Author / Work	Noise Type	Method	SNR Improvement (dB)
Awal et al[1].	AWGN	S-median	1.4896
		MABWT	7.80
		WT	6.50
Jenkal et al.[13]	WGN	ADWT	9.40
		MABWT (Multi-Adaptive Bionic Wavelet Transform)	7.80
Lu et al. [10]	WGN	W-EMD	7.79
		M-EMD	9.82
Martens et al.[2]	Power line 50 Hz	Notch filter	16.5752
Leski & Henzel [8]	Baseline wander	Low-pass filter	14.8204
Antczak [6]	Mainly AWGN	DRNN (deep recurrent NN)	≈ 7.71
Rifai et al.[7]	BW + MA + EM	1D CNN autoencoder	15.80
Proposed work (this paper)	**WGN + 50 Hz + Baseline wander**	**DWT (bior6.8)**	**18.3215**

Although deep-learning methods such as DRNN and 1D CNN autoencoders achieve competitive performance [6, 7], they require extensive training data and computational resources, whereas the proposed DWT-based method is lightweight and more suitable for real-time applications.

5.4. Challenges and Limitations of the Proposed Architecture

The suggested DWT-based structure effectively minimizes noise, but it still has limits. It currently operates in offline mode, processing the entire ECG after it's recorded. We have not implemented live broadcast capabilities or online changes. This needs additional planning about handling delays, storage and hardware. However, the proposed architecture was implemented using MATLAB/Simulink tools that enable future hardware implementation on FPGA using Xilinx System Generator for DSP.

a. Computational Complexity and Real-Time Analysis

The computational cost of the proposed architecture is mainly determined by the convolution operations within the multilevel DWT and the subband filtering applied to d_2 and d_3. If the wavelet filter has length L, a single convolution requires approximately L multiplications and $L-1$ additions per output sample. The filters involved in the computation of the DWT usually have equal length L. This is true in the orthogonal case, while in the biorthogonal case the filter lengths may differ by a few samples only. In this study the case of equal filter lengths is realized. If lengths differ, one can pad the filter coefficients with zeros. The DWT and IDWT require just the same number of operations (multiplications and additions) per sample. When expanding the DWT to multiple levels, the computation complexity will depend on the number of levels J. At each DWT stage, the downsampling of the splitting step reduces the number of approximation coefficients to half the number of input samples from the preceding stage [5, 44]. Across three analysis levels and three synthesis levels $J = 3$, the DWT stages require about $L(2 + 1 + 1/2) = 7L/2$ multiplications per sample and $7L/2$ additions per sample. As shown in Fig. 16, the analysis low pass filter $h_0(k)$ with length L is connected after the details d_2 output. Since this at the second level has input subsampled by $2^2 = 4$. Therefore, the number of operations are $L/4$ multiplications per sample and $(L-1)/4$ additions per sample. While, at level 3, input is subsampled by $2^3 = 8$, and a cascade $g_0(k)$ and $g_1(k)$ filters are connected after d_3. Therefore, the number of operations is $L/8$ multiplications per sample and $(L-1)/8$ additions per sample for each filter. For the implementation of 8 levels cascade DWT, decimators $h_0(k)$ downsample by 2; the number of operations (multiplications and additions) per sample are $L(1-2^{-8}) \approx L$ multiplications per sample and $(L-1)(1-2^{-8}) \approx L-1$ additions per sample. The same number of operations (multiplications and additions) per sample are required for 8-level cascade IDWT interpolators $g_0(k)$ up sample by 2. However, in the design proposed in Fig. 16, the approximated output a_3 is already computed by the 3-level DWT stages. Therefore, only the required computation complexity for levels 4 to 8 of cascade decimators $h_0(k)$. Therefore, the number of

operations are $L - 7L/8 = L/8$ multiplications per sample and $(L-1)/8$ additions per sample. Table 9 shows the resulting total complexities for different parts of the proposed architecture in Fig. 17 using a direct convolutional-based approach, while Table 10 reports the complexities for wavelet filters with different lengths L.

Table 9. Arithmetic complexity per sample for different parts of the proposed architecture in Fig. 17 using direct convolution-based approach.

Number of operations per sample	**3-level DWT**	**3-level IDWT**	$\mathbf{h_0(k)}$ after d_2	$\mathbf{g_0(k)}, \mathbf{g_1(k)}$ after d_3	**Levels 4–8** $h_0(k)$	**8-level** $g_0(k)$	**Total**
Multiplication	$\frac{7L}{2}$	$\frac{7L}{2}$	$\frac{L}{4}$	$\frac{L}{4}$	$\frac{L}{8}$	L	$8.625L$
Addition	$\frac{7(L-1)}{2}$	$\frac{7(L-1)}{2}$	$\frac{L-1}{4}$	$\frac{L-1}{4}$	$\frac{L-1}{8}$	$(L-1)$	$8.625(L-1)$

Table 10. The resulting complexities for some wavelet filter types with different lengths L.

Number of operations per sample	**fk8,** $L = 8$	**db8,** $L = 16$	**sym8,** $L = 16$	**bior6.8,** $L = 18$	**coif5,** $L = 30$
Multiplication	69	138	138	155.25	258.75
Addition	60.375	129.375	129.375	146.625	250.125

As shown in Table 10, a trade-off exists among the evaluated wavelet filters, where the *bior6.8* wavelet provides a balanced compromise between computational cost and denoising performance. For the bior6.8 wavelet (with the longest filter length $L = 18$), the computational cost corresponds to approximately 155 multiplications and 147 additions per sample.

In general, for processing N samples of the input signal, the total number of multiplication and addition operations are approximately $8.625NL$ and $8.625N(L-1)$, respectively.

b. Latency and Buffering Considerations

The proposed architecture in Fig. 17 is implemented using MATLAB/Simulink environment tools that process the input signal serially on a sample-by-sample basis and produce the output at the sampling rate f_s. Therefore, the structure of the proposed architecture is independent of the signal length, making it efficient and suitable for real-time processing. The computational latency is equal to the sampling period T_s ($T_s = 1/f_s$), corresponding to one output per clock cycle.

For the analysis and synthesis stages, at any synthesis stage, the reconstructed approximation and detail data streams are merged to produce the output, as shown in Fig. 3. Consequently, a delay is introduced between the reconstructed output and the corresponding detail data streams, and these delays must be properly aligned. To ensure perfect reconstruction of the DWT–IDWT scheme in real time, the delays of the various filter paths must be equalized. The delays defined in (11), $D_j = (2^{J-j} - 1)(L-1)$, are used to equalize the multistage filter bank.

Considering that the sampling period of the input signal at level $j = 0$ is T_s, the effective sampling rate increases dyadically by a factor of 2^j after each decomposition level. Therefore, the inherent delay for subsequent levels $1 \le j \le J$ can be computed at each level using (11), as summarized in Table 11 for a wavelet filter of length L with $J = 8$.

Table 11. Delay equalization for 8 levels ($J = 8$).

j	1	2	3	4	5	6	7	8
D_j	$127(L-1)$	$63(L-1)$	$31(L-1)$	$15(L-1)$	$7(L-1)$	$3(L-1)$	$(L-1)$	0

As shown in Fig. 17, h_0 is connected to d_2, and h_0 produces a delay D_{h_0}. To compensate for this delay, it should be subtracted from D_1. The average group delay is used to evaluate the delay caused by the filter; thus, the corresponding equalized delay is $D_2 - D_{h_0}$. In addition, the cascade filters g_0 and g_1 are connected to d_3, producing a delay $D_{g_0g_1}$, and the corresponding equalized delay is $D_3 - D_{g_0g_1}$.
Consequently, the total time delay latency between the input signal and the reconstructed signal can be determined by considering the input signal at level $j = 0$. Substituting in (11), the delay is obtained as $D_0 = 255(L-1)$. To compute the equalized delay for Fig. 16 with the bior6.8 wavelet ($L = 18$), the subsequent delays are listed in Table 12. The resulting time-delay latency between the input and output is approximately $D_0T_s = 4335T_s = 4335/f_s = 12$ s for $f_s = 360$ Hz.

Table 12. The equalized time delays of the different paths for the proposed architecture using the bior6.8 wavelet.

j	0	1	2	3	8
Group delay	–	–	$D_{h_0} = 9$	$D_{g_0g_1} = 17$	–
D_j	4335	2159	1062	510	0

The model of the proposed architecture in Fig. 17 is implemented using MATLAB/Simulink (2022b). The model uses only delay block buffers and does not require any additional memory or buffer blocks.

6. Conclusion and Future Work

This study presents a single DWT-based architecture for efficient ECG signals denoising. The proposed method effectively removes multiple types of the noise, including baseline noise, power line interference and white Gaussian noise, within a unified architecture. Experimental evaluations demonstrated that the proposed architecture outperforms traditional denoising methods, achieving higher signal-to-noise ratio (SNR) improvements and stronger correlation with original clean ECG signals. Specifically, correlation coefficients increased up to 0.9832, and SNR improvements reach to 17.97 dB, highlighting the robustness of the approach through the different noise types. The result confirms that this architecture provides a reliable and efficient solution for ECG denoising, which can enhance the accuracy of cardiac arrhythmia diagnosis and support following signal processing or automatic examination.

Future work will focus on advancing the proposed architecture toward real-time implementation and adaptation for wearable and ambulatory ECG monitoring systems. Although the proposed method effectively suppresses baseline wander, power-line interference, and white Gaussian noise, motion artifacts remain a significant challenge, particularly in wearable settings where such disturbances often overlap with the QRS complex and other diagnostically relevant components. To address this limitation, future studies will investigate enhanced motion artifact mitigation strategies, including accelerometer-assisted adaptive filtering, signal-dependent wavelet thresholding, and hybrid frameworks that integrate the proposed DWT approach with adaptive filtering or empirical mode decomposition (EMD). These developments aim to achieve more selective artifact suppression while preserving critical ECG morphology. In addition, the proposed architecture will be implemented on a lightweight FPGA platform to enable online, real-time ECG denoising. This implementation will allow evaluation of latency, throughput, and resource utilization, thereby confirming the feasibility of deploying the method in hardware-constrained environments such as wearable medical devices.

Data and Code Availability

The source code developed in this work is publicly available on GitHub at: https://github.com/Shelan83/ECG_Denoising_Project.

Acknowledgement

This paper has been supported by Duhok Polytechnic University, the University of Duhok, and my supervisors. I am grateful for their wonderful assistance in providing me with ongoing advice and assistance throughout my research also, the authors would like to thank the PhysioNet community for providing access to the MIT-BIH Arrhythmia Database and the Noise Stress Test Database, which were essential for conducting this research.

REFERENCES

1. Md. Abdul Awal, Sheikh Shanawaz Mostafa, Mohiuddin Ahmad, and Mohd Abdur Rashid, *An adaptive level dependent wavelet thresholding for ECG denoising*, Biocybernetics and Biomedical Engineering, vol. 34, no. 4, pp. 238–249, 2014.
2. S. M. M. Martens, M. Mischi, S. G. Oei, and J. W. M. Bergmans, *An improved adaptive power line interference canceller for electrocardiography*, IEEE Transactions on Biomedical Engineering, vol. 53, no. 11, pp. 2220–2231, Nov. 2006.
3. D. L. Donoho, *De-noising by soft-thresholding*, IEEE Transactions on Information Theory, vol. 41, no. 3, pp. 613–627, 1995.
4. M. A. Awal, S. S. Mostafa, and M. Ahmad, *Performance analysis of wavelet-based ECG denoising techniques*, International Journal of Electrical and Computer Engineering, vol. 1, no. 3, pp. 328–334, 2011.
5. O. Rioul and P. Duhamel, *Fast algorithms for discrete and continuous wavelet transforms*, IEEE Transactions on Information Theory, vol. 38, no. 2, pp. 569–586, 1992.
6. K. Antczak, *Deep recurrent neural networks for ECG signal denoising*, 2018.
7. A. Rifai, M. N. Rachmatullah, and W. K. Sari, *ECG signal denoising using 1D convolutional neural network*, Computer Engineering and Applications, vol. 13, no. 2, pp. 60–68, 2024.
8. J. M. Łeski and N. Henzel, *ECG baseline wander and powerline interference reduction using nonlinear filter bank*, Signal Processing, vol. 85, no. 4, pp. 781–793, Apr. 2005.
9. S. Poungponsri and X. H. Yu, *Electrocardiogram (ECG) signal modeling and noise reduction using wavelet neural networks*, in Proc. IEEE Int. Conf. Automation and Logistics (ICAL), 2009, pp. 394–398.
10. Y. Lu, J. Yan, and Y. Yam, *Model-based ECG Denoising Using Empirical Mode Decomposition*.
11. M. Blanco-Velasco, B. Weng, and K. E. Barner, *ECG signal denoising and baseline wander correction based on the empirical mode decomposition*, Computers in Biology and Medicine, vol. 38, no. 1, pp. 1–13, Jan. 2008.
12. Y. Der Lin and Y. H. Hu, *Power-line interference detection and suppression in ECG signal processing*, IEEE Transactions on Biomedical Engineering, vol. 55, no. 1, pp. 354–357, Jan. 2008.
13. W. Jenkal, R. Latif, A. Toumanari, A. Dliou, O. El B'Charri, and F. M. R. Maoulainine, *An efficient algorithm of ECG signal denoising using the adaptive dual threshold filter and the discrete wavelet transform*, Biocybernetics and Biomedical Engineering, vol. 36, no. 3, pp. 499–508, 2016.
14. H. Y. Lin, S. Y. Liang, Y. L. Ho, Y. H. Lin, and H. P. Ma, *Discrete-wavelet-transform-based noise removal and feature extraction for ECG signals*, IRBM, vol. 35, no. 6, pp. 351–361, Dec. 2014.
15. N. Verma and A. K. Verma, *Performance analysis of wavelet thresholding methods in denoising of audio signals of some Indian musical instruments*.
16. T. Ben Jabeur, E. Bashier, Q. Sandhu, K. J. Bwalya, and A. Joshua, *Noise and artifacts elimination in ECG signals using wavelet, variational mode decomposition and nonlocal means algorithm*.
17. J. Kubicek, M. Penhaker, and R. Kahankova, *Design of a synthetic ECG signal based on the Fourier series*, in Proc. Int. Conf. Advances in Computing, Communications and Informatics (ICACCI), IEEE, Nov. 2014, pp. 1881–1885.
18. Á. Ádám, D. Val'ko, Z. Balogh, B. Madoš, and J. Hurtuk, *Comparative evaluation of filtration techniques for ECG signal denoising with emphasis on stationary wavelet transform*, Scientific Reports, vol. 15, no. 1, p. 42514, 2025.
19. Y. Zhang, K. Yu, C. Huang, R. Qu, Z. Fan, P. Zhu, et al., *Adaptive layer-dependent threshold function for wavelet denoising of ECG and multimode fiber cardiorespiratory signals*, Sensors, vol. 25, no. 24, p. 7644, 2025.
20. A. Azzouz, B. Bengherbia, P. Wira, N. Alaoui, A. Souahlia, M. Maazouz, and H. Hentabeli, *An efficient ECG signals denoising technique based on the combination of particle swarm optimisation and wavelet transform*, Heliyon, vol. 10, no. 5, 2024.
21. M. Raggi and L. Mesin, *Denoising the ECG from the EMG using stationary wavelet transform and template matching*, Electronics, vol. 14, no. 17, p. 3474, 2025.
22. P. Zhu, L. Feng, K. Yu, Y. Zhang, W. Chen, and J. Hao, *Enhanced DWT for denoising heartbeat signal in non-invasive detection*, Sensors, vol. 25, no. 6, p. 1743, 2025.
23. M. B. Mohiuddin and I. Janajreh, *Analysis and synthesis of electrocardiogram (ECG) using Fourier and wavelet transform*, International Journal of Thermal & Environmental Engineering, vol. 17, no. 2, pp. 85–97, 2020.
24. B. R. Manju and B. Akshaya, *Simulation of Pathological ECG Signal Using Transform Method*, Procedia Computer Science, Elsevier, 2020, pp. 2121–2127.
25. R. Karthik and T. H. Semester, *ECG Simulation Using MATLAB Principle of Fourier Series*.
26. B. Zanchi et al., *Synthetic ECG signals generation: A scoping review*, Computers in Biology and Medicine, Elsevier, Jan. 2025.
27. A. Kheirati Roonizi and R. Sassi, *ECG signal decomposition using Fourier analysis*, EURASIP Journal on Advances in Signal Processing, vol. 2024, no. 1, Dec. 2024.
28. A. Majkowski, M. Kołodziej, and R. J. Rak, *Joint time-frequency and wavelet analysis – An introduction*, Metrology and Measurement Systems, vol. 21, no. 4, pp. 741–758, Dec. 2014.
29. F. Samann, S. A. Bamerni, J. A. Khorsheed, and A. K. Al-Sulaifanie, *Adaptive real-time wavelet denoising architecture based on feedback control loop*, Journal of Engineering Research, vol. 9, ICRIE, 2021.

30. F. Samann and T. Schanze, *An efficient ECG denoising method using discrete wavelet with Savitzky–Golay filter*, in *Current Directions in Biomedical Engineering*, Walter de Gruyter GmbH, Sep. 2019, pp. 385–387.
31. S. G. Mallat, *A theory for multiresolution signal decomposition: The wavelet representation*, 1987.
32. A. N. Saleh and A. K. Al-Sulaifanie, *Real time VLSI IWT denoising architecture*, The Journal of The University of Duhok, vol. 20, no. 1, pp. 164–174, Jul. 2017.
33. M. Bahoura and H. Ezzaidi, *FPGA-implementation of wavelet based denoising technique to remove power-line interference from ECG signal*, in Proc. 10th IEEE Int. Conf. Information Technology and Applications in Biomedicine, Corfu, 2010.
34. Z. Germán-Salló, *Nonlinear filtering in ECG signal denoising*, 2010.
35. Z. K. Peng, M. R. Jackson, J. A. Rongong, F. L. Chu, and R. M. Parkin, *On the energy leakage of discrete wavelet transform*, Mechanical Systems and Signal Processing, vol. 23, no. 2, pp. 330–343, Feb. 2009.
36. O. Br, D. Maq, A. Cce, and V. Filho, *Dynamical model for generating synthetic ECG signals*, 2018.
37. S. K. Mitra, *Digital Signal Processing: A Computer-Based Approach*, 3rd ed.
38. T. Saramäki and R. Bregović, *Multirate systems and filter banks*.
39. L. Milić, *Multirate filtering for digital signal processing: MATLAB applications*, Information Science Reference, 2009.
40. T.-H. Yi and X.-Y. Zhang, *Noise smoothing for structural vibration test signals using an improved wavelet thresholding technique*, Sensors, 2012.
41. D. L. Donoho and I. M. Johnstone, *Adapting to unknown smoothness via wavelet shrinkage*, 1991.
42. B. Ergen, *Signal and image denoising using wavelet transform*, InTech Open Access Publisher, 2012.
43. M. Misiti, Y. Misiti, G. Oppenheim, and J.-M. Poggi, *Wavelet Toolbox™ User's Guide*, MathWorks, 1997.
44. A. K. Al-Sulaifanie, A. Ahmadi, and M. Zwolinski, *Very large-scale integration architecture for integer wavelet transform*, IET Computers & Digital Techniques, vol. 4, no. 6, pp. 471–483, 2010.
45. D. Gede, H. Wisana, C. Nugraha, and R. A. Rachman, *Development of a low-cost and efficient ECG devices with IIR digital filter design*, Indonesian Journal of Electronics, Electromedical, and Medical Informatics (IJEEEMI), vol. 3, no. 1, pp. 21–28, 2021.
46. R. Kher, *Signal processing techniques for removing noise from ECG signals*, 2019.
47. G. B. Moody and R. G. Mark, *The impact of the MIT-BIH Arrhythmia Database*, IEEE Engineering in Medicine and Biology Magazine, vol. 20, no. 3, pp. 45–50, May–Jun. 2001.